Verification of Convection-Allowing Model Ensemble Analyses of Near-Storm Environments Using MPEX Upsonde Observations

CHRISTOPHER A. KERR

School of Meteorology, Cooperative Institute for Mesoscale Meteorological Studies, University of Oklahoma, and NOAA/National Severe Storms Laboratory, Norman, Oklahoma

DAVID J. STENSRUD

Department of Meteorology and Atmospheric Science, The Pennsylvania State University, University Park, Pennsylvania

XUGUANG WANG

School of Meteorology, University of Oklahoma, Norman, Oklahoma

(Manuscript received 27 July 2016, in final form 2 November 2016)

ABSTRACT

The Mesoscale Predictability Experiment (MPEX) conducted during the spring of 2013 included frequent coordinated sampling of near-storm environments via upsondes. These unique observations were taken to better understand the upscale effects of deep convection on the environment, and are used to validate the accuracy of convection-allowing ($\Delta x = 3$ km) model ensemble analyses. A 36-member ensemble was created with physics diversity using the Weather Research and Forecasting Model, and observations were assimilated via the Data Assimilation Research Testbed using an ensemble adjustment Kalman filter. A 4-day sequence of convective events from 28 to 31 May 2013 in the south-central United States was analyzed by assimilating Doppler radar and conventional observations. No MPEX upsonde observations were assimilated. Since the ensemble mean analyses produce an accurate depiction of the storms, the MPEX observations are used to verify the accuracy of the analyses of the near-storm environment.

A total of 81 upsondes were released over the 4-day period, sampling different regions of near-storm environments including storm inflow, outflow, and anvil. The MPEX observations reveal modest analysis errors overall when considering all samples, although specific environmental regions reveal larger errors in some state fields. The ensemble analyses underestimate cold pool depth, and storm inflow meridional winds have a pronounced northerly bias that results from an underprediction of inflow wind speed magnitude. Most bias distributions are Gaussian-like, with a few being bimodal owing to systematic biases of certain state fields and environmental regions.

1. Introduction

Convection-allowing models (CAMs) have been found to be very valuable to improved predictions of the organization and evolution of convection (e.g., Kain et al. 2006, 2008; Clark et al. 2010a,b). Reliable forecasts of deep convection are needed to improve warnings for associated high-impact meteorological phenomena (e.g., damaging winds, flash flooding, hail, tornadoes; Stensrud et al. 2009, 2013). The practical predictability of such events is largely dependent on having accurate initial conditions and small model error (Zhang et al. 2007; Cintineo and Stensrud 2013). Results from Cintineo and Stensrud (2013) suggest that convective environments must be well represented by the models to ensure reasonable forecast accuracy. Thus, one facet that must be well depicted is the impact of long-lived convection on the environment (i.e., upscale feedbacks). Proper depictions of these feedbacks should lead to better short-term forecasts. The largest hindrance to evaluating the accuracy of model analyses of near-storm environments is the lack of sufficient observations to perform such studies.

Corresponding author e-mail: Christopher A. Kerr, christopher.kerr@ou.edu

DOI: 10.1175/MWR-D-16-0287.1

The Mesoscale Predictability Experiment (MPEX) included frequent, coordinated sampling of near-storm environments during 15 May–15 June 2013 across the U.S. Great Plains using radiosondes (also called upsondes or sondes) (Weisman et al. 2015; Trapp et al. 2016; Hitchcock et al. 2016). These upsondes provided vertical profiles of temperature, humidity, pressure, and zonal and meridional wind components at a variety of nearby locations relative to areas of deep convection and thus should have sampled the upscale feedbacks from convection on the nearby mesoscale environment. While many previous studies have demonstrated the impacts of deep convection on the surrounding environment through either model simulations (e.g., Maddox 1980; Fritsch and Maddox 1981b; Brooks et al. 1994; Stensrud 1996; Stensrud and Anderson 2001) or observations (e.g., Fritsch and Maddox 1981a; Parker 2014), the number of near-storm environment observations has been limited causing extensive verification to be neglected.

Mesoscale convective systems (MCSs) are known to be a cause of upper-tropospheric meso-α-scale anticyclones (Ninomiya 1971a,b; Maddox 1980; Fritsch and Maddox 1981a,b; Anabor et al. 2009; Trier and Sharman 2009; Metz and Bosart 2010). With these anticyclones, 200-hPa winds and geopotential heights can be perturbed by over 20 m s^{-1} and 80 m, respectively (Leary 1979; Fritsch and Maddox 1981a,b; Perkey and Maddox 1985; Smull and Augustine 1993). These perturbations often are observed relatively soon after the convective event (6–24 h; Weisman et al. 2015). Jet streaks have also been shown to be enhanced due to the presence of MCSs (Keyser and Johnson 1984; Wolf and Johnson 1995a,b). Simulated supercells increase storm-relative environmental helicity (SREH) and convective available potential energy (CAPE) within convective inflow regions (Brooks et al. 1994). Low-level inflow to deep convection also increases if the convection is persistent (Stensrud 1996).

Although many studies have described the impacts of deep convection on the large-scale environment, few have focused on nearby mesoscale environmental impacts and the accuracy of numerical weather models' depictions of these alterations. Numerous studies have shown that CAMs can successfully simulate the structure of convection via radar data assimilation (e.g., Snyder and Zhang 2003; Dowell et al. 2004; Yussouf et al. 2013, 2015; Johnson et al. 2015). However, does radar data assimilation with a CAM provide sufficient information for storm-scale model analyses to reasonably represent the changes in the near-storm environment from convective feedbacks? Using upsonde observations collected from near-storm environments during MPEX, a more complete evaluation of model ensemble analysis accuracy within the environments surrounding deep convection is performed. This evaluation is done in order to assess whether the numerical model's depiction of the environments influenced by convection is reasonable. This evaluation will reveal any systematic biases and model errors within the convectively perturbed environment that could influence subsequent predictions of convective evolution.

The next section describes the events of interest from MPEX and the corresponding upsonde operations. Section 3 outlines the model configuration and data assimilation experiments. Results are presented in section 4 with a discussion and conclusions in section 5.

2. MPEX upsonde operations and convective events

Four mobile upsonde units operated during MPEX to sample preconvective (PDE strategy) and near-storm environments that were convectively disturbed (CDE; Weisman et al. 2015; Trapp et al. 2016). These units were from the National Severe Storms Laboratory (NSSL), Purdue University, Colorado State University (CSU), and Texas A&M University (TAMU). NSSL, Purdue, and TAMU used radiosondes manufactured by International Met Systems (iMet) while CSU made use of Vaisala radiosondes. The differences in observation error and data quality between these two radiosonde systems are negligible (Trapp et al. 2016). Sondes were carried by 200-g latex balloons that could ascend above the tropopause, having maximum flight times of approximately 1 h. During CDE sampling, observations were collected in convective inflow, convective outflow, and anvil regions among others.

The four convective events highlighted in this study occurred during 28–31 May 2013 in portions of Texas, Oklahoma, and Kansas. Forcing for convection initiation generally stemmed from drylines, with modest large-scale forcing resulting from a cyclonic vorticity maximum ejecting into the central United States. All four MPEX upsonde units targeted a diminishing thunderstorm cluster in the Oklahoma Panhandle moving into southern Kansas on 28 May. The units predominantly sampled the downstream environment at fixed locations, beginning at 2000 UTC in a rectangular formation, to measure environmental changes as convection approached their locations (Fig. 1a). The final sonde was released around 0030 UTC 29 May. An example of simultaneously released upsonde profiles show how a realistic convective environment can vary over short distances (<150 km; Fig. 2). The NSSL and TAMU launches were approximately 115 km apart, but TAMU observed a stout capping inversion while NSSL—located closer to the dryline—did not. The following day (29 May) featured a developing squall line in the Texas Panhandle that eventually translated into

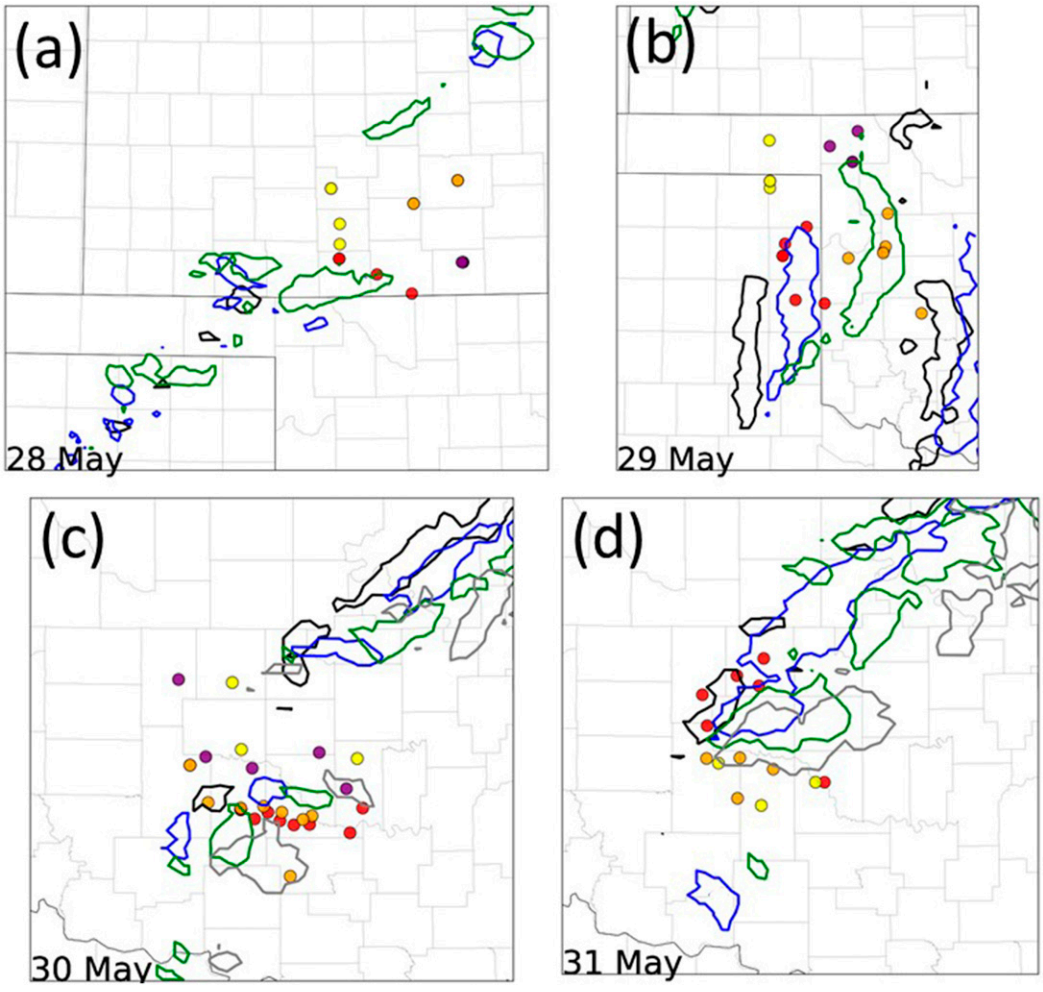

FIG. 1. Hourly observed reflectivity 30-dBZ contours for (a) 2100 (black), 2200 (blue), and 2300 (green) UTC 28 May; (b) 2100 (black), 2200 (blue), and 2300 (green) UTC 29 May; (c) 1900 (black), 2000 (blue), 2100 (green), and 2200 (gray) UTC 30 May; and (d) 2200 (black) and 2300 (blue) UTC 31 May, and 0000 (green) and 0100 (gray) UTC 1 Jun. MPEX upsonde releases are denoted with circles [NSSL (red), Purdue (orange), CSU (yellow), and TAMU (purple)].

western Oklahoma. Upsondes were released in the wake of the squall line and sampled the environment around a bookend vortex on the convective line's northern edge (Fig. 1b). Deployments shifted to central Oklahoma for 30 and 31 May, where supercell thunderstorms were targeted. The inflow region of a nontornadic supercell was sampled every 30 min for several hours on 30 May by NSSL, while the three other units sampled the convective wake and environment to the north of this predominately eastward-moving supercell (Fig. 1c). NSSL, Purdue, and CSU sampled the tornadic supercell that produced a large tornado near El Reno, Oklahoma, on 31 May (Bluestein et al. 2015). As in the previous day, both inflow and wake regions were sampled frequently (Fig. 1d).

Over this 4-day period, a total of 81 upsondes were released. It should be noted that some upsondes did not ascend very far above 600 hPa after release for a variety of reasons (interference with convection, balloon burst, etc.), so only the profiles below upsonde termination are used for verification. Manual quality control also was applied to the entire upsonde dataset. The estimated accuracies of the upsonde observations are 0.5 K for temperature, 5% for relative humidity, 1 m s^{-1} for the zonal and meridional wind components, and 1 hPa for pressure between the surface and tropopause.

3. Experimental design

The 4-day sequence chosen is simulated using the Advanced Research version of the Weather Research and Forecasting Model (WRF-ARW), version 3.4.1 (Skamarock et al. 2008). A nested domain is placed over

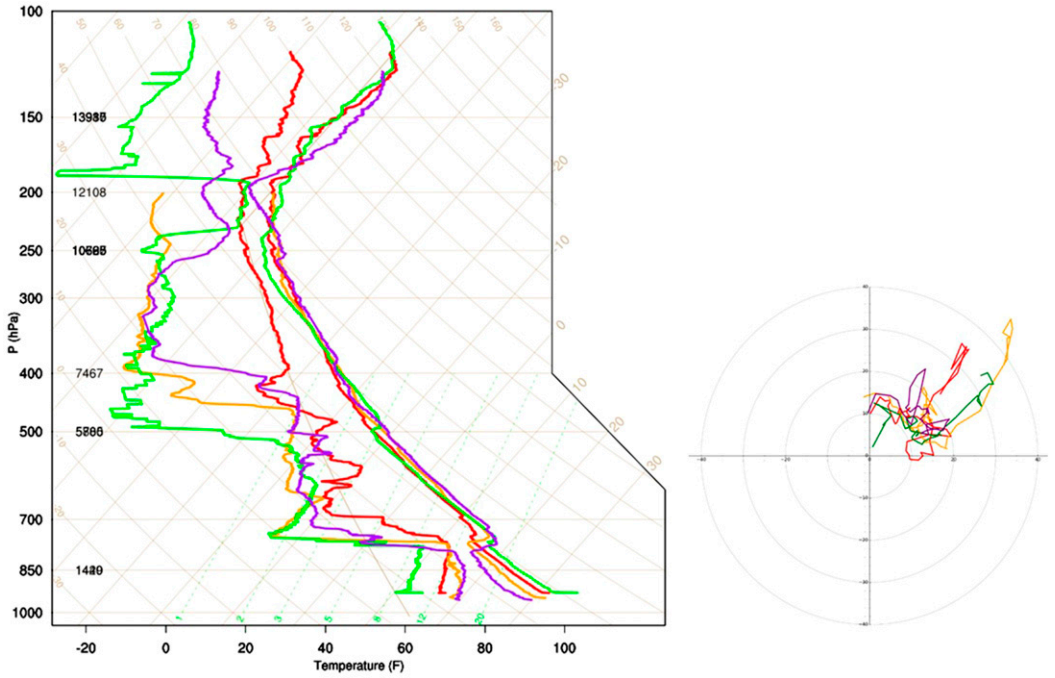

FIG. 2. 2100 UTC 28 May MPEX sounding skew T–log p thermodynamic profiles and hodographs with NSSL (red), Purdue (orange), CSU (green), and TAMU (purple).

portions of Texas, Oklahoma, and Kansas in order to encompass all targeted convection during the 28–31 May period. This inner domain has a horizontal grid spacing of 3 km while the outer domain (CONUS) has a grid spacing of 15 km (Fig. 3). Both domains used 51 vertical layers from the surface to 10 hPa. The NSSL Experimental Warn-on-Forecast (WoF) System for ensembles (NEWS-e) is utilized (Wheatley et al. 2015; Jones et al. 2016). This 36-member ensemble is initialized at 0000 UTC each respective day using a downscaled

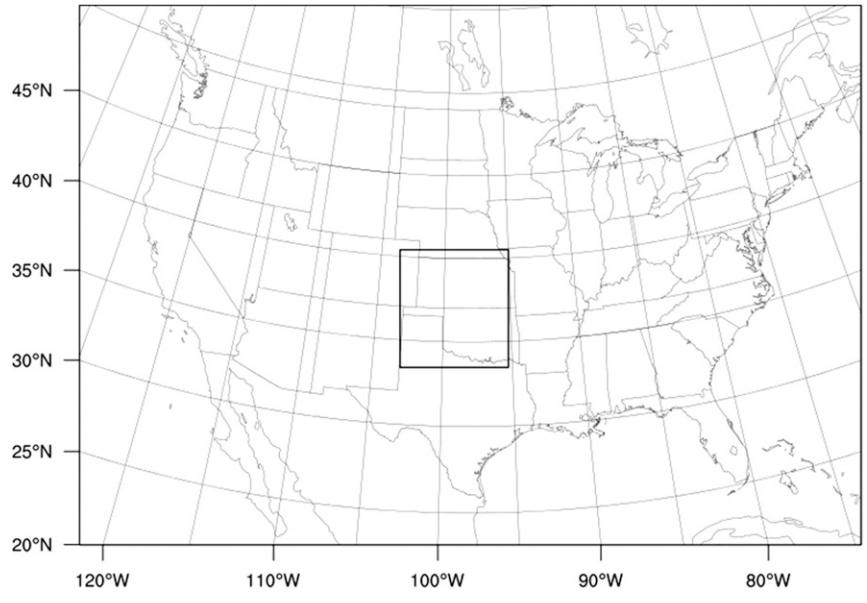

FIG. 3. Outer model domain (CONUS; 15-km grid spacing) and nested, convection-resolving domain (3-km grid spacing), which includes KS, OK, and the TX Panhandle.

21-member Global Ensemble Forecast System (GEFS). The boundary conditions for the outer domain are also created using the GEFS. The outer domain serves as the boundary conditions for the inner domain.

Ensemble members are developed following Wheatley et al. (2015) using a combination of 18 GEFS members and 18 physics combinations of planetary boundary layer (PBL), longwave and shortwave radiation, and convective (outer domain only) parameterization schemes (Table 1). Members 1–18 are initialized with the corresponding GEFS member (member 1 with GEFS member 1, member 2 with GEFS member 2, etc.) and are run with the corresponding numerical physics combination from Table 1. Members 19–36 are initialized with the same 18 GEFS members in descending order (member 19 with GEFS member 18, member 20 with GEFS member 17, etc.) while running the physics combinations in ascending order (member 19 with combination 1, member 20 with combination 2, etc.) All ensemble members use the Thompson et al. (2008) microphysics scheme. Since there are only 18 unique initial conditions at 0000 UTC (due to only 18 GEFS members), the model is integrated 1 h forward to 0100 UTC each day to create 36 unique initial conditions.

TABLE 1. Physics options applied to 18 GEFS members. This set of physics options also is applied to these same 18 GEFS members in reverse order to create members 19–36 (e.g., member 19 is initialized with GEFS member 18 but has physics option 1 applied). The Thompson microphysics and RAP land surface parameterization is applied to all members. PBL schemes include the Yonsei University (YSU), Mellor–Yamada–Janjić (MYJ), and Mellor–Yamada–Nakanishi–Niino (MYNN) schemes. Shortwave (SW) and longwave (LW) radiation schemes include the Dudhia shortwave scheme, Rapid Radiative Transfer Model (RRTM) shortwave scheme, and the Rapid Radiative Transfer Model–Global (RRTMG) shortwave and longwave schemes (adapted from Wheatley et al. 2015).

Member	PBL	SW radiation	LW radiation	Cumulus
1	YSU	Dudhia	RRTM	Kain–Fritsch
2	YSU	RRTMG	RRTMG	Kain–Fritsch
3	MYJ	Dudhia	RRTM	Kain–Fritsch
4	MYJ	RRTMG	RRTMG	Kain–Fritsch
5	MYNN	Dudhia	RRTM	Kain–Fritsch
6	MYNN	RRTMG	RRTMG	Kain–Fritsch
7	YSU	Dudhia	RRTM	Grell
8	YSU	RRTMG	RRTMG	Grell
9	MYJ	Dudhia	RRTM	Grell
10	MYJ	RRTMG	RRTMG	Grell
11	MYNN	Dudhia	RRTM	Grell
12	MYNN	RRTMG	RRTMG	Grell
13	YSU	Dudhia	RRTM	Tiedtke
14	YSU	RRTMG	RRTMG	Tiedtke
15	MYJ	Dudhia	RRTM	Tiedtke
16	MYJ	RRTMG	RRTMG	Tiedtke
17	MYNN	Dudhia	RRTM	Tiedtke
18	MYNN	RRTMG	RRTMG	Tiedtke

a. Mesoscale data assimilation

Hourly cycles of mesoscale data assimilation begin at 0100 UTC, when the first analysis is created. Conventional observations of temperature, dewpoint, pressure, and zonal and meridional wind components, provided by the NOAA/Meteorological Assimilation Data Ingest System (MADIS), are assimilated using an ensemble adjustment Kalman filter (EAKF) available via the Data Assimilation Research Testbed (DART; Anderson 2001; Anderson et al. 2009). These observations platforms include METAR and marine surface stations, the Aircraft Communications Addressing and Reporting System (ACARS), and rawinsondes along with data from MADIS mesonet and the Oklahoma Mesonet. The MPEX upsonde observations are not assimilated.

The Gaspari and Cohn (1999) Gaussian-like localization function is utilized for all observations assimilated. The horizontal localization cutoff for nonmesonet mesoscale observations is approximately 458 km with a vertical localization cutoff of 8 km [consistent with Wheatley et al. (2012, 2015)]. Mesonet observations have a horizontal localization of approximately 60 km [consistent with Sobash and Stensrud (2015), Wheatley et al. (2015), and Jones et al. (2016)]. Ensemble spread is maintained using spatial and temporal prior adaptive inflation (Anderson 2007).

b. Storm-scale data assimilation

At a predetermined time based on each day's convective event (Table 2), storm-scale data assimilation begins. Level-II radar data (radar reflectivity and radial velocity; radars for each event listed in Table 2) are assimilated every 15 min along with MADIS mesonet, Oklahoma Mesonet, and conventional rawinsonde observations. As with the outer domain, no MPEX observations are assimilated. The horizontal localization cutoff for radar observations is 18 km with a 6-km vertical cutoff (Yussouf et al. 2013; Wheatley et al. 2014, 2015; Jones et al. 2016). Surface and conventional rawinsonde observations retain the identical localization specifications as used in mesoscale data assimilation. This assimilation only updates the inner domain as the parent domain continues to serve as lateral boundary conditions without update from data assimilation. Radar reflectivity observations less than 10 dBZ are considered clear-air reflectivity observations and set to 0 dBZ (Wheatley et al. 2015). Radial velocity observations are only assimilated if they are collocated with reflectivity observations exceeding or equal to 20 dBZ.

TABLE 2. Description of the convective events each day. The start and end times of radar data assimilation are listed with the corresponding radars that collected the data including Dodge City, KS (KDDC); Amarillo, TX (KAMA); Vance Air Force Base, OK (KVNX); Wichita, KS (KICT); Oklahoma City, OK (KTLX); and Frederick, OK (KFDR). The number of MPEX upsondes released during each event is listed last.

Date	Event	Radars	Start time	End time	Upsondes
28 May	Oklahoma Panhandle; southern Kansas thunderstorm cluster	KDDC, KICT, KAMA, KVNX	1900 UTC	0200 UTC (29 May)	18
29 May	Texas Panhandle; western Oklahoma bow echo and bookend vortex	KAMA, KFDR, KDDC, KVNX	1700 UTC	2345 UTC	20
30 May	Central Oklahoma nontornadic supercell	KTLX, KFDR	1700 UTC	2300 UTC	28
31 May	Central Oklahoma tornadic supercell	KTLX, KFDR, KVNX	2100 UTC	0230 UTC (1 June)	15

After quality control of radar observations, the data are objectively analyzed to a 6-km Cartesian grid using the Cressman scheme (Cressman 1959) via the Observation Processing and Wind Synthesis (OPAWS; Majcen et al. 2008) software. Radar observations collected within a 15-min window centered on the analysis time are assimilated. Observation errors of 5 dBZ for radar reflectivity and 3 m s^{-1} for radial velocity are assumed uniform and constant throughout each experiment (Dowell et al. 2004; Aksoy et al. 2009; Yussouf et al. 2013, Wheatley et al. 2015; Jones et al. 2016). Convection spinup is induced by the additive noise technique developed by Dowell and Wicker (2009). Perturbations are added to the temperature, dewpoint, and horizontal wind fields in each member at locations where the reflectivity innovations are >10 dBZ and reflectivity observations are >25 dBZ (Sobash and Wicker 2015).

The 15-min storm-scale data assimilation cycling continues until a predetermined ending time that is unique to each experiment (Table 2). The ending times are based on the end of MPEX upsonde operations. High-resolution (Δx = 3 km) ensemble analyses are thus available every 15 min from convection initiation to the end of MPEX operations for each of the four cases. MPEX upsonde observations are windowed to the closest 15-min analysis time to the upsonde release time. All observations collected by each sonde are considered valid at this analysis time. Ensemble sounding profiles are created for each MPEX upsonde by linearly interpolating the ensemble analysis output to the horizontal sonde location at logarithmically interpolated 25-hPa vertical increments. Windowing each observation throughout the flight did not result in statistically significant differences (not shown).

4. Results

A subjective evaluation of the analyses rendered with radar data assimilation indicate that the 15-min ensemble mean analyses reproduce the structures of supercells, squall lines, and other convective features as seen in earlier studies (Snyder and Zhang 2003; Dowell et al. 2004; Tong and Xue 2005; Aksoy et al. 2009, 2010; Yussouf and Stensrud 2010). The ensemble mean reflectivity analyses show that the depictions of the targeted convection on each day compare reasonably to reflectivity observations (Figs. 4a–d). Further evidence of radar data assimilation effectiveness is shown by the root-mean-square error (RMSE) and total ensemble spread from 28 May (Figs. 4e,f), which illustrate how radial velocity and reflectivity assimilation has positive impacts on ensemble mean analyses. Similar behaviors are seen in the other three cases and indicate that the ensemble data assimilation system is producing a reasonable analysis of the ongoing convection.

a. Near-storm environment analysis errors

The ensemble mean analyses of the near-storm environment are evaluated using diagnostics with the special MPEX observations of temperature, relative humidity, and zonal and meridional wind components. Vertical profiles of the root-mean-square difference (RMSD) are calculated using samples over the 4-day period and is defined as

$$\mathrm{RMSD} = \sqrt{\frac{1}{N}\sum_{n=1}^{N}(x_a^n - x_o^n)^2},$$

where x_a^n is the ensemble mean analysis, x_o^n is observation, and N is the number of observations collected at the respective pressure level over the 4-day period. Mean ensemble spread (MES) is defined as

$$\mathrm{MES} = \frac{1}{N}\sum_{n=1}^{N}\sqrt{\sigma_{\mathrm{obs}}^2 + \frac{1}{35}\sum_{i=1}^{36}(\overline{x}_a - x_{ia})^2},$$

where i is ensemble member, σ_{obs}^2 is observation error variance, $\overline{x}_a$ is ensemble mean analysis, x_{ia} is ensemble member analysis, and N is the number of observations. Another diagnostic is mean bias of the analyses (MB), defined as

$$\mathrm{MB} = \frac{1}{N}\sum_{n=1}^{N}(x_a^n - x_o^n),$$

where x_a^n, x_o^n, and N are previously defined.

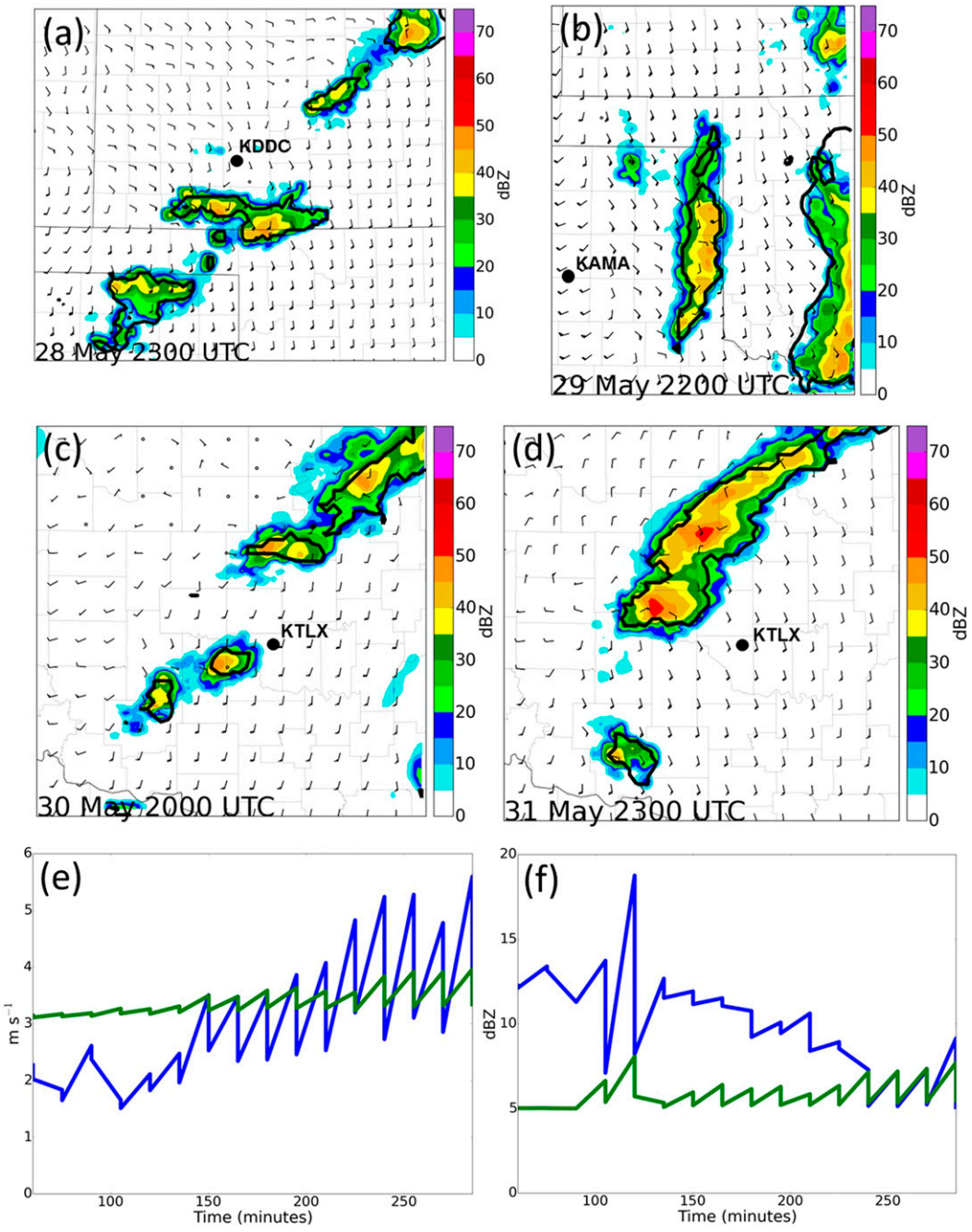

FIG. 4. Examples of low-level ensemble mean analysis reflectivity and surface winds (kt, barbs) with observed 20-dBZ reflectivity outlined with solid black line, at 0.5° tilt by the designated radar: (a) 2300 UTC 28 May (KDDC), (b) 2200 UTC 29 May (KAMA), (c) 2000 UTC 30 May (KTLX), and (d) 2300 UTC 31 May (KTLX). Example of (e) radial velocity and (f) reflectivity sawtooth diagrams show ensemble mean prior and posterior RMSE (blue) and ensemble total spread (green) from 28 May with time (min) after storm-scale assimilation begins.

The pressure-dependent sample size (Fig. 5a) has a magnitude of 81 between 925 and 850 hPa. The sample size generally decreases with height due to a variety of sonde and/or balloon failures. At 500 hPa, the sample size is 70. The sample size continues to decrease, reaching only 11 at 100 hPa. As previously stated, upsondes were released in a variety of regions surrounding the targeted convection including inflow, anvil, and outflow. Inflow soundings are designated as those released in areas where ground-relative low-level winds

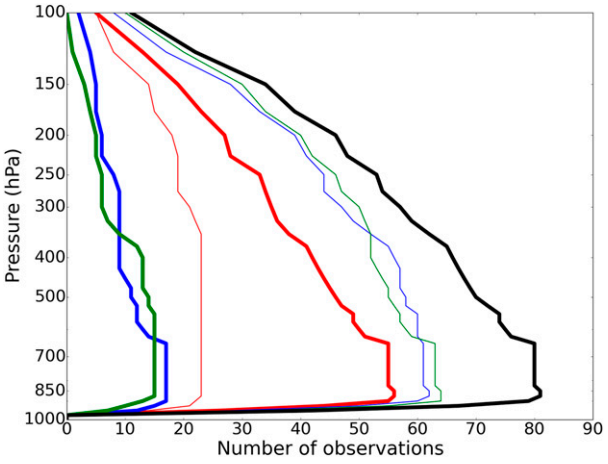

FIG. 5. Number of MPEX upsonde samples with height during 28–31 May. All (black), inflow (thick blue), noninflow (thin blue), outflow (thick green), nonoutflow (thin green), anvil (thick red), and nonanvil (thin red).

are directed into the region of convection. Anvil regions are areas under upper-level cloud produced by convection, including instances where inflow soundings sampled the storm anvil in upper levels. Outflow environments are mainly confined to upstream (relative to storm motion) cold pool regions along with surging outflow ahead of convective cells. The upsonde counts for individual regions within the near-storm environments (Fig. 5) show a modest sample size for inflow and outflow regions (17 and 15 upsondes, respectively). A majority of upsondes were released within anvil regions (56 upsondes).

The RMSD of ensemble mean temperature for all 81 samples (Fig. 6a) reveals a local maximum just below 850 hPa of approximately 2 K. While the MB (Fig. 6b) does not show a local maximum at this height, the MES below 850 hPa exceeds 6 K. Inspection of individual soundings suggests that this RMSD maximum is caused by the analyses failing to accurately capture the capping inversion strength, as also seen in Coniglio et al. (2013). Another local RMSD maximum of ~1.75 K is seen at 500 hPa in association with a local extreme in MB of ~−1 K, part of a midlevel cold bias that is present across all regions. Inspection of individual observed upsondes often reveals the presence of weak to moderate stable layers at the top of the elevated mixed layer (as in the CSU and TAMU soundings in Fig. 2). These features are not captured by the analyses, which tend to have smooth vertical temperature profiles, contributing to the midlevel cold bias. The largest RMSD, MES, and MB are in upper levels near the tropopause. Temperatures near the tropopause have large spatial variations, as seen in Fig. 2 where upsondes were released within 150 km of each other. Significant horizontal gradients in tropopause temperature lead to larger RMSDs and MBs as well as large MES due to ensemble variability.

For inflow soundings, observations reveal a small warm bias of approximately 1 K from the surface up to 600 hPa that slowly transitions to a negative bias by 500 hPa (Figs. 6c,d). In contrast, outflow analyses have a large warm MB of slightly less than 2 K in low levels (near 850 hPa; Figs. 6e,f), corresponding to a very large RMSD of approximately 4 K at the same pressure level. This warm bias is unique to outflow regions since it does not appear in nonoutflow regions. The pronounced warm bias and RMSD maximum in these low levels is due to the analysis cold pools being warmer than observed, as also suggested by Engerer et al. (2008). This result also suggests cold pools are too shallow in the ensemble analyses. Some outflow samples are considered anvil as well (Figs. 6g,h), where the inclusion of outflow samples is the source of the RMSD maximum near 850 hPa for these two regions. The anvil region MES in upper levels of the troposphere increases dramatically, signifying large temperature ensemble variations within thunderstorm anvils.

Relative humidity RMSDs for all upsondes increase with height, beginning near 6% at 925 hPa and increasing to approximately 18% between 850 and 700 hPa (Fig. 7a). MB magnitudes are less than 10% below 500 hPa, suggesting that low-level relative humidity analyses are reasonable (Fig. 7b). RMSD and MB continue to increase into the midlevels (~400 hPa) reaching ~25% and ~13%, respectively, and the values of RMSD tend to remain fairly constant until the tropopause. Inspection of a number of upsonde humidity profiles suggests that the larger RMSDs and MBs in mid- to upper levels likely are due in part to either the presence or absence of observed moist layers combined with smooth ensemble analyses and large MES. As Fig. 2 suggests, moist layers have well-defined tops where relative humidity decreases rapidly with height. Therefore, small vertical displacement errors in the locations of the moist layers produce large RMSDs. The upsondes also have a known issue measuring humidity when RH is <20%, a common occurrence in upper levels of the troposphere (Sapucci et al. 2005), which contributes to the large positive MB and large RMSD values above 400 hPa. Large RMSD and, by comparison, small MB below 700 hPa, result from a large variance in analysis errors among samples. This result is evidenced by MES between 850 and 700 hPa, where the MES magnitude approaches 80%.

The RMSDs of zonal and meridional winds for all upsondes reveal relatively small analysis errors in low levels (Figs. 8a and 9a). The zonal wind RMSD is less

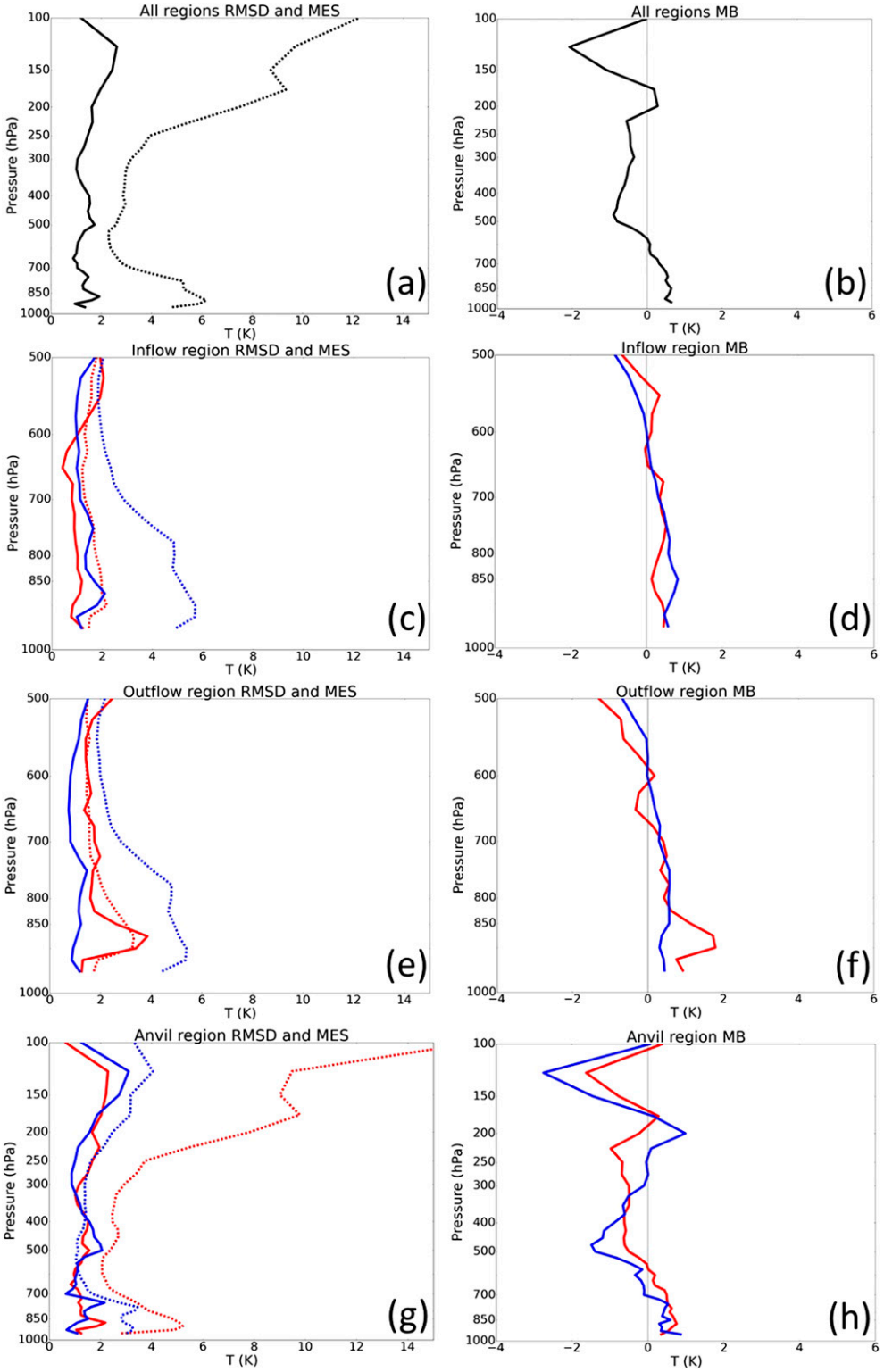

FIG. 6. Vertical profiles of temperature (T) (left) root-mean-square difference (RMSD, solid) and mean ensemble spread (MES, dashed), and (right) mean bias (MB, solid). (a) All upsonde RMSD and MES, 1000–100 hPa; (b) all upsonde MB, 1000–100 hPa; (c) inflow (red) and noninflow (blue) RMSD and MES, 1000–500 hPa; (d) inflow (red) and noninflow (blue) MB, 1000–500 hPa; (e) outflow (red) and nonoutflow (blue) RMSD and MES, 1000–500 hPa; (f) outflow (red) and nonoutflow (blue) MB, 1000–500 hPa; (g) anvil (red) and nonanvil (blue) RMSD and MES, 1000–100 hPa; and (h) anvil (red) and nonanvil (blue) MB, 1000–100 hPa.

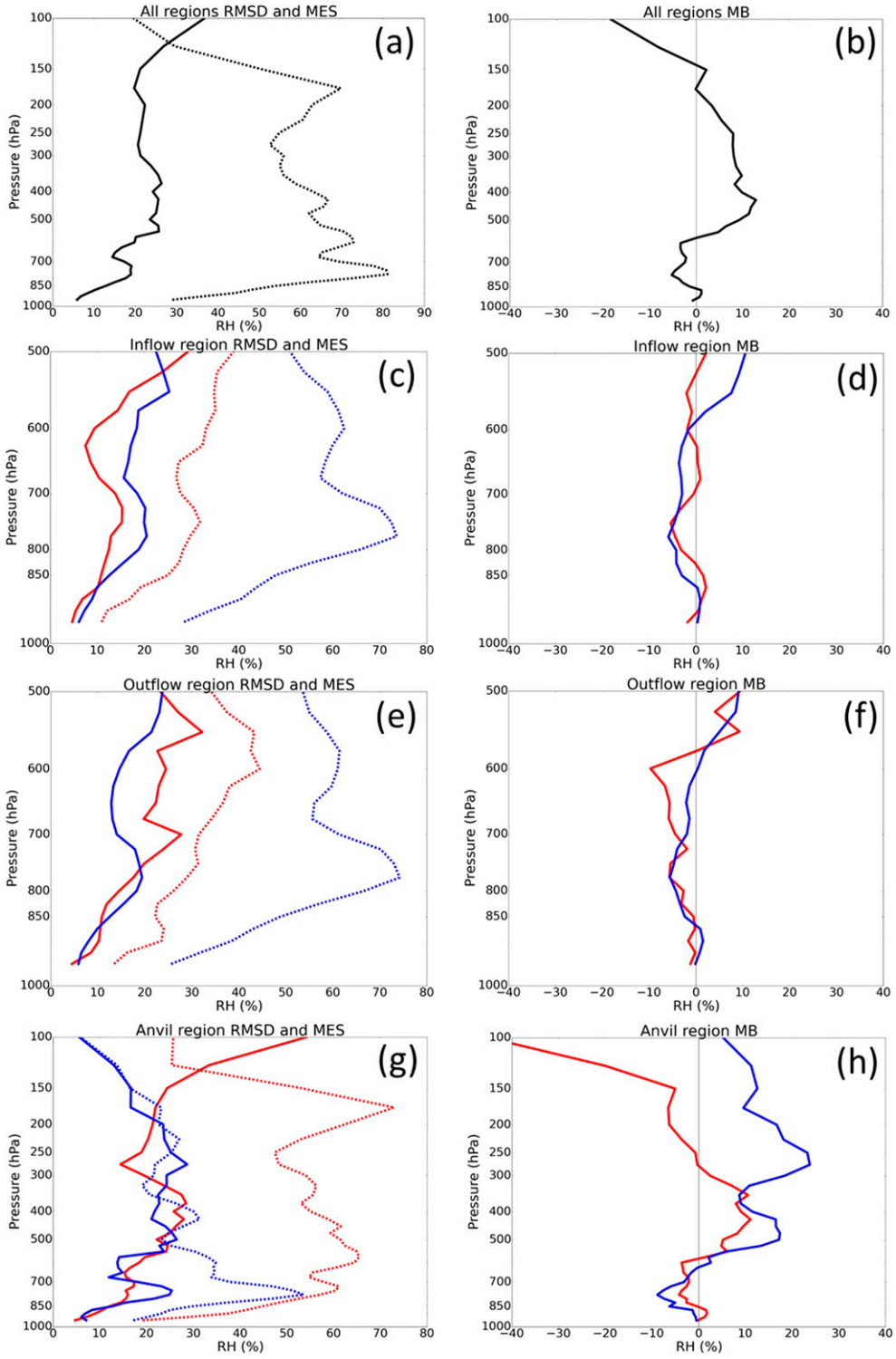

FIG. 7. As in Fig. 6, but for relative humidity (RH).

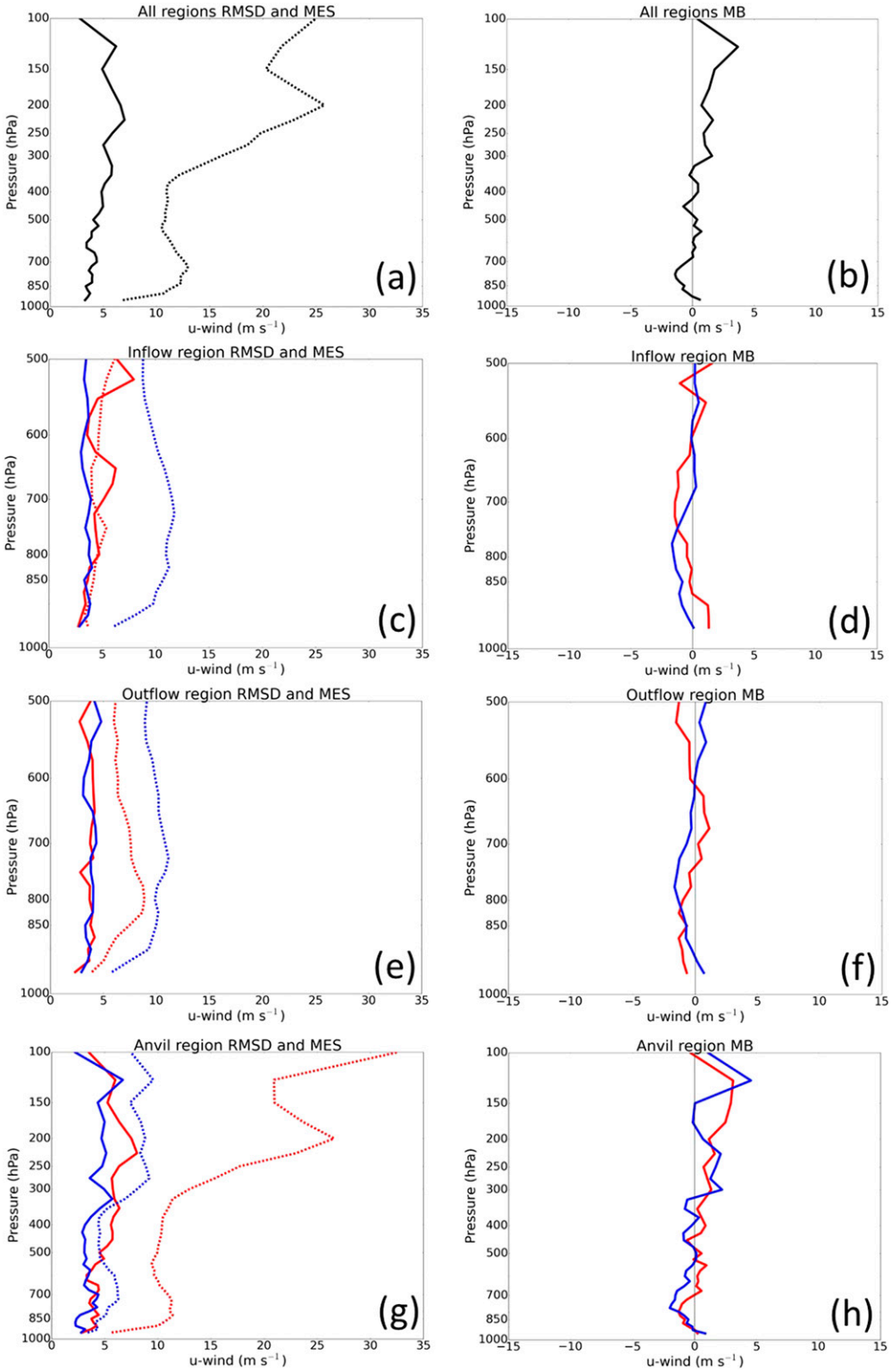

FIG. 8. As in Fig. 6, but for zonal winds (u wind).

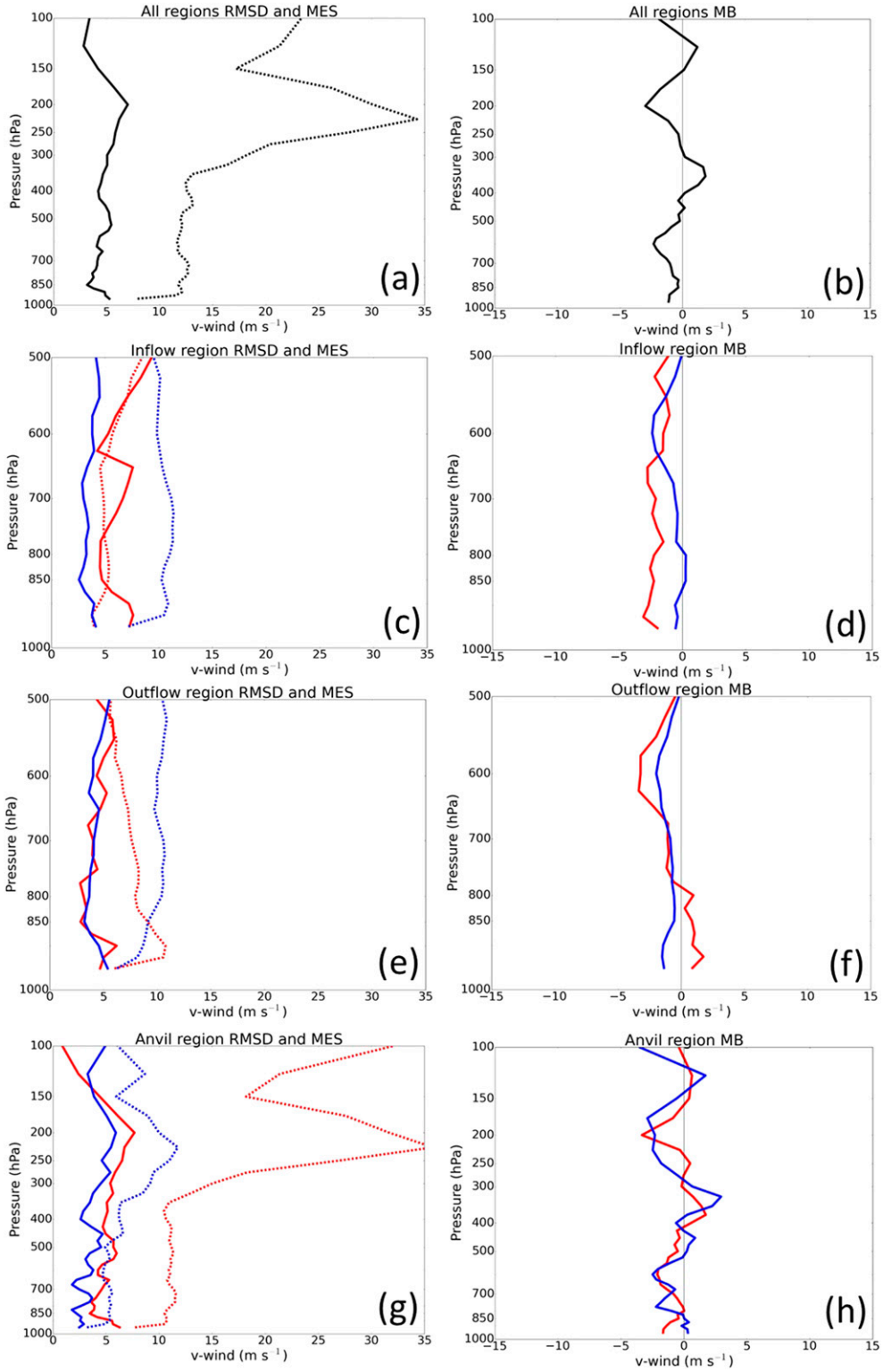

FIG. 9. As in Fig. 6, but for meridional winds (v wind).

than 5 m s^{-1} below 450 hPa but slowly and steadily increases until 225 hPa. The zonal mean MB (Fig. 8b) oscillates around 0 m s^{-1} in the low to midlevels and is strictly positive above ~325 hPa. Meridional winds also have RMSDs less than 5 m s^{-1} above 925 hPa and below 500 hPa. Both the zonal and meridional winds have a local RMSD maximum in the upper levels of the troposphere near 200 hPa, with the zonal wind having a small positive MB and the meridional wind having a larger negative MB. This finding is associated with large MES within thunderstorm anvils for both zonal and meridional winds (Figs. 8g and 9g). An encouraging result arises from the inflow region zonal wind below 500 hPa, where MB oscillates between −2 and 2 m s^{-1} throughout that vertical depth (Fig. 8d). However, the inflow region meridional wind has negative MBs for the entire depth with magnitudes reaching ~3 m s^{-1} and RMSDs at or above 5 m s^{-1} (Figs. 9c,d). The northerly bias indicates an underprediction of inflow wind speeds into the convective region given the strong southerly component associated with storm inflow in the supercell cases of 30 and 31 May. The noninflow region results show smaller meridional wind RMSDs in low to midlevels than found in the inflow region by comparison.

Wind speed for all upsondes is negatively biased in the analyses from the surface to 400 hPa (Fig. 10b). A negative wind speed maximum in MB occurs at 200 hPa. This maximum is collocated with a negative meridional wind MB at 200 hPa (Fig. 9b), which produces the negative wind speed bias along with some directional error. A comparison of wind components in the 150–100-hPa layer shows the zonal wind to be slightly overestimated while the meridional wind MB is near 0. The inflow region low-level wind speeds are underpredicted much more so than low-level noninflow region wind speeds (Fig. 10d). Outflow wind speed MB is similar to noninflow MB (Fig. 10f). The large MES is once again present within upper levels of anvil regions (Fig. 10g).

Another environmental parameter conducive for convection includes vertical wind shear. The RMSDs of surface–700-hPa and surface–500-hPa wind shear are 5.9 and 4.5 m s^{-1}, respectively (Table 3). Magnitudes of MB for both layers are quite small (−0.8 and −0.3 m s^{-1}, respectively). The large RMSD and small MB imply a large variance among samples. Model analyses reveal steep shear gradients near convection (not shown), which would induce large variances when spatial errors are present. Of all near-storm environment regions, inflow regions have the largest RMSDs for both surface–700-hPa and surface–500-hPa wind shear. All other regions are very comparable to the overall values previously mentioned. The MBs of all regions except inflow are comparable as well. Inflow surface–700-hPa MB is notably larger in magnitude (negative value) since the meridional winds analyses have a notable northerly bias.

b. Bias distributions

Histograms are used to show the distribution of biases for different state fields. At pressure levels where there are large magnitudes of RMSD and/or MB, these distributions may shed light on bias characteristics. Biases of each ensemble member for each sample are calculated for selected variables at specified pressure levels. The resulting bias distribution for 875-hPa temperature is Gaussian-like with a maximum on the positive side of zero and more bias samples >4 than <−4 K (Fig. 11a).

Another Gaussian distribution is suggested in the relative humidity errors at 750 hPa (Fig. 11b). However, the peak of the distribution is near +5%. As the magnitude of the MB increases, there are generally more negative samples than their positive counterparts. The 225-hPa zonal wind field reveals a bimodal distribution where one peak is near zero and a second peak is between 5 and 10 m s^{-1} (Fig. 11c). It should be noted that there are many samples of extremely large bias magnitude (>15 m s^{-1}), indicating large differences with some ensemble members. A histogram of 200-hPa meridional wind bias also has a bimodal distribution (Fig. 11d). However, the two maximums are near zero and between −5 and −10 m s^{-1}.

c. Physics-dependent errors

Figure 12 depicts differences in MB and RMSD among ensemble members that differ in their physics as described in Table 1. The nested domain physics has variations in PBL scheme (i.e., 3) and shortwave/longwave radiation scheme combinations (i.e., 2; see Table 1). Temperature biases below approximately 600 hPa are largely dependent on PBL scheme (Figs. 12a,b). The YSU PBL scheme results in larger warm biases below 850 hPa and smaller warm biases between 850 and 600 hPa compared to the other schemes. When combined with results with relative humidity (Figs. 12c,d), where the YSU scheme has a dry bias below 850 hPa and a moist bias above 850 hPa, the data suggest that YSU produces boundary layers that are too deep. Dry biases above 850 hPa for MYJ and MYNN PBL schemes suggest boundary layers that are too shallow (Hong et al. 2006; Coniglio et al. 2013). The MYJ PBL scheme has the smallest bias in temperature and relative humidity below 850 hPa. Members utilizing the Dudhia–RRTM radiation scheme combination also have a slight warm bias compared to its RRTMG scheme counterpart below 850 hPa. However, the Dudhia–RRTM combination is slightly cooler than RRTMG between 850 and 600 hPa. No significant

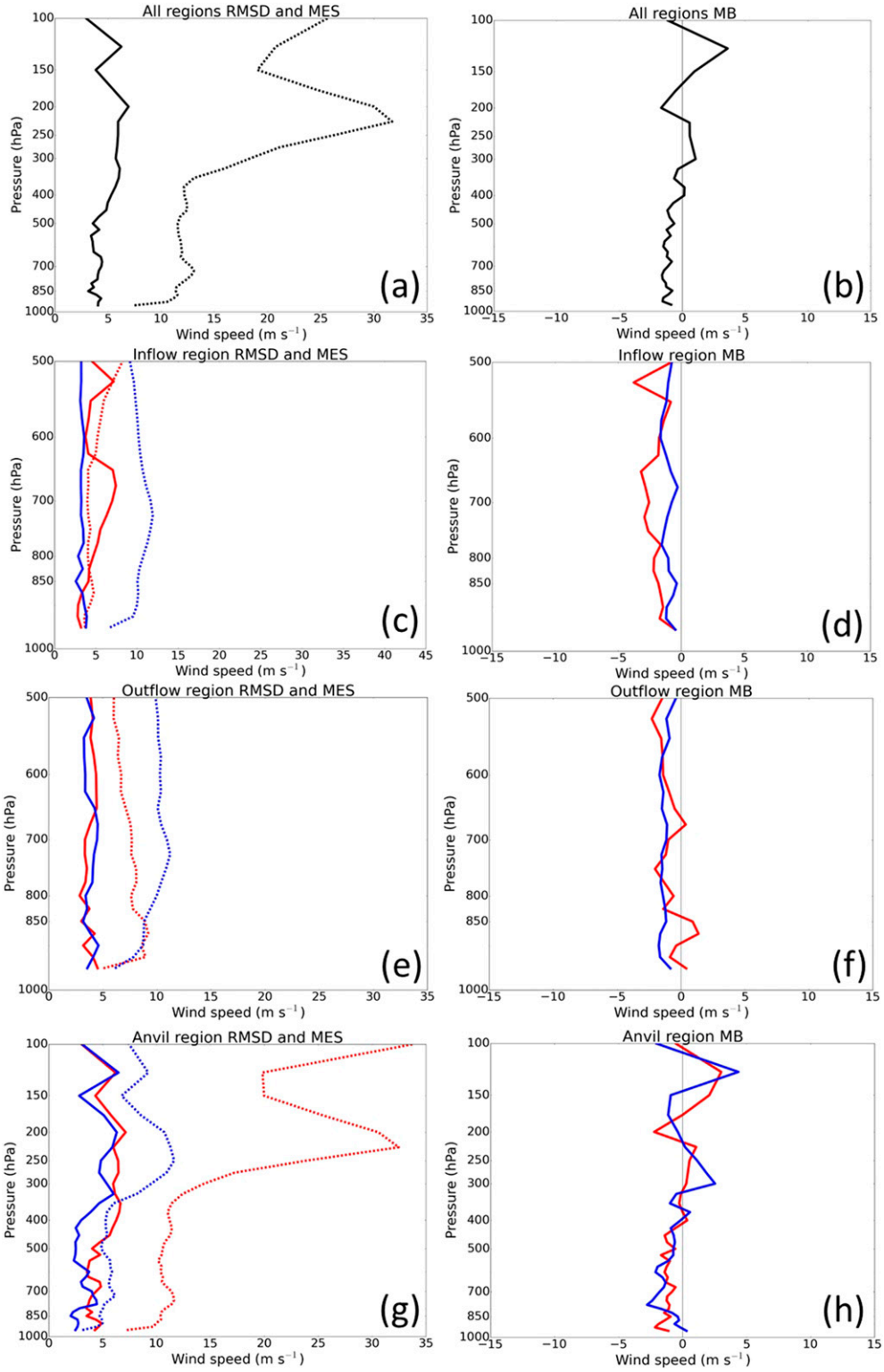

FIG. 10. As in Fig. 6, but for wind speed.

TABLE 3. Surface–700-hPa and surface–500-hPa wind shear RMSD and MB for all upsondes and each individual near-storm environment region. All RMSDs and MBs are in m s^{-1}. The number of shear observations within each region is listed last.

Region	Surface–700-hPa count	Surface–700-hPa RMSD	Surface–700-hPa MB	Surface–500-hPa count	Surface–500-hPa RMSD	Surface–500-hPa MB
All	80	5.9	−0.8	70	4.5	−0.3
Inflow	17	7.2	−4.2	11	6.8	−1.3
Noninflow	63	5.2	−0.2	59	4.3	−0.4
Outflow	15	5.0	−0.3	14	4.1	−0.4
Nonoutflow	65	6.1	−1.1	56	5.1	−0.3
Anvil	57	6.0	−0.4	47	5.2	0.1
Nonanvil	23	5.7	−2.0	23	4.4	−1.1

differences in temperature are seen between radiation physics options above 600 hPa.

The effects of PBL schemes (mainly YSU) extend farther into the midtroposphere in all fields except temperature. MYJ has the driest bias between 800 and ~550 hPa. Radiation schemes do not have as great of an effect on relative humidity bias. The Dudhia–RRTM combination has a slight dry bias over RRTMG below 850 hPa. Horizontal wind fields are negligibly affected by physics schemes (Figs. 12e–h). However, MYJ PBL scheme seems to have a more negative bias over YSU and MYNN in mid- to upper levels within the zonal wind field while causing a more positive bias within the meridional wind field.

5. Discussion and conclusions

Over this 4-day period, a total of 81 upsondes were released nearby deep convection in a variety of storm-relative locations. The decreasing sample size with

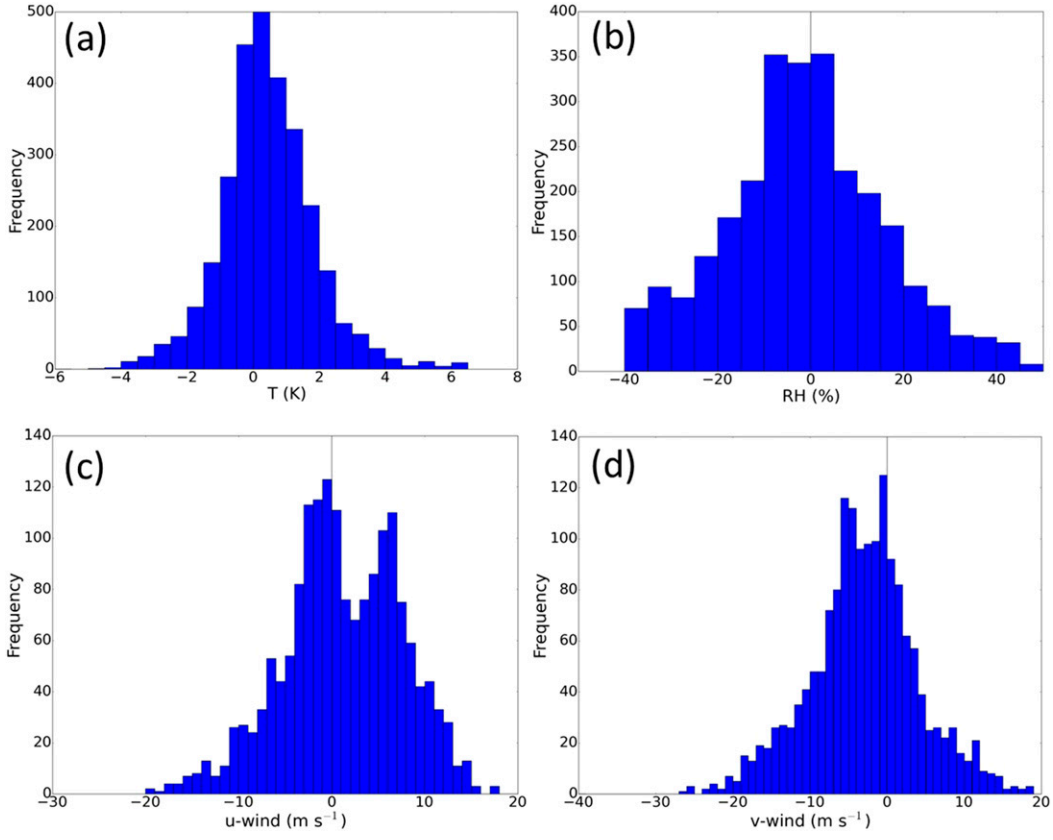

FIG. 11. Individual ensemble member bias histograms where frequency is number of ensemble member biases over all 81 samples (2916 total) for (a) 875-hPa temperature with 0.5-K bins, (b) 750-hPa relative humidity with 5% bins, (c) 225-hPa u wind with 1 m s^{-1} bins, and (d) 200-hPa v wind with 1 m s^{-1} bins.

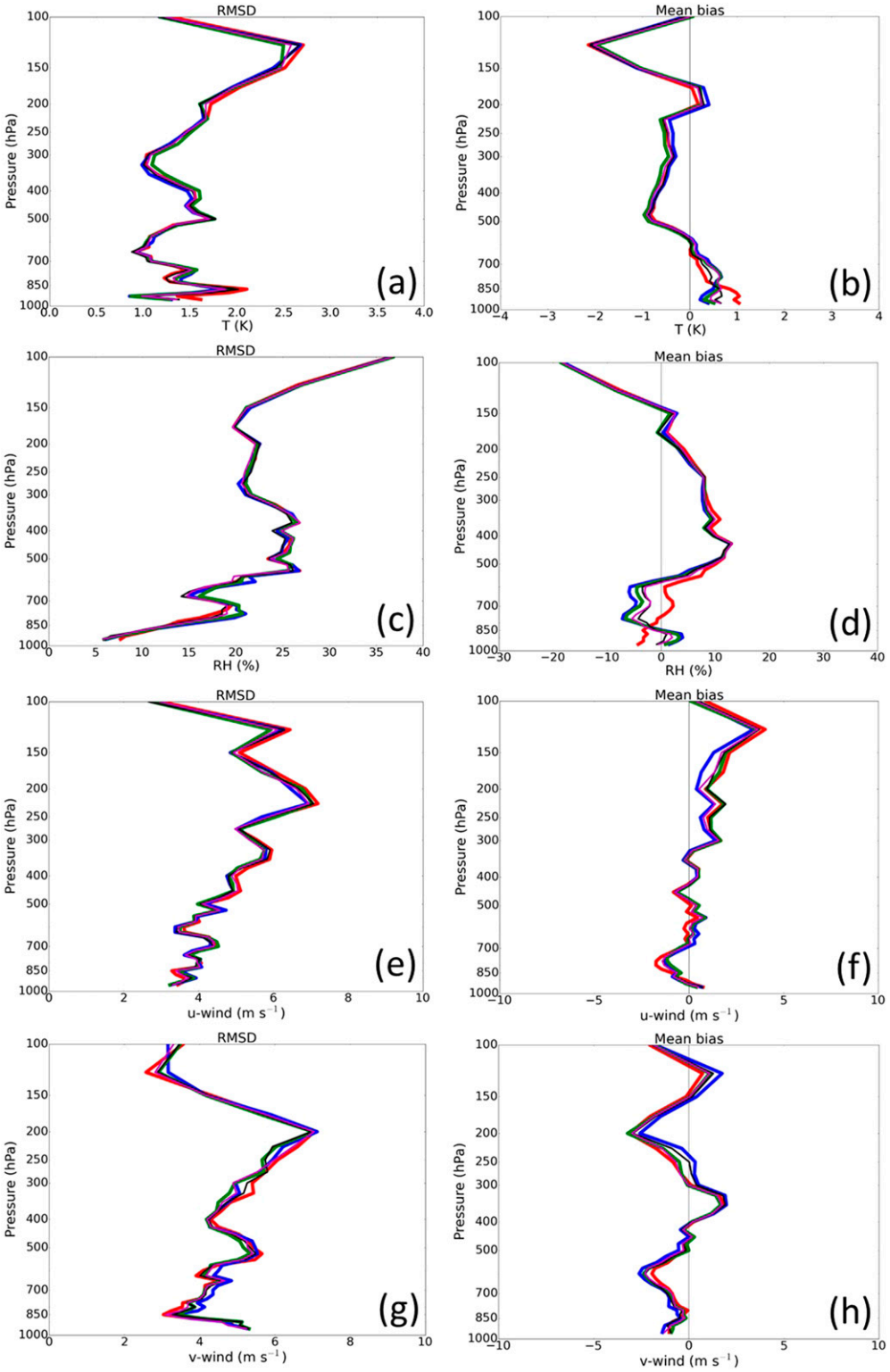

FIG. 12. RMSD and MB for mean of members with specific physics schemes [YSU PBL (red), MYJ PBL (blue), MYNN PBL (green), Dudhia–RRTM combination (black), RRTMG combination (magenta)]. Profiles are for (a) temperature RMSD, (b) temperature MB, (c) relative humidity RMSD, (d) relative humidity MB, (e) *u*-wind RMSD, (f) *u*-wind MB, (g) *v*-wind RMSD, and (h) *v*-wind MB.

height obviously weakens conclusions made within the upper troposphere, especially in near-storm environment regions with small sample sizes. Nonetheless, the special MPEX observations revealed that WRF-ARW ensemble mean analyses at CAM grid spacing agree reasonably well with the observed convective near-storm environments over this 4-day sequence, with some notable exceptions.

1) A large variance in analysis temperature bias is implied by a maximum of RMSD in temperature just below 850 hPa. This is likely in part a result of model analyses improper handling of capping inversions at the top of the PBL (not shown), which were present in many sounding datasets. The choice of PBL schemes is found to greatly impact the low-level temperature analyses. This has previously been presented by Coniglio et al. (2013) where model temperatures in preconvective environments are highly dependent on PBL scheme.
2) The outflow region upsondes reveal a large warm bias in the analyses near 850 hPa. Further inspection of individual soundings shows that the ensemble analyses have warmer temperatures than observed, a result consistent with the conclusions of Engerer et al. (2008). Since cold pools are important to the evolution of deep convection (Rotunno et al. 1988; Weisman and Rotunno 2004), this result deserves further attention as it could impact forecast accuracy.
3) The negative temperature MB in upper levels is a result of horizontal temperature gradients near the tropopause not being accurately captured by the analyses. Errors in horizontal temperature gradient placements cause RMSD and MB magnitudes to increase. Overall, near-storm temperatures are well depicted in the ensemble analyses considering the lack of conventional mesoscale temperature profile observations.
4) Relative humidity MB is consistently between ±10% below 500 hPa in all regions nearby deep convection. However, relative humidity RMSD increases with height and is above 20% by 500 hPa. The midlevel relative humidity errors appear to be due to smooth ensemble analyses and errors in dry and moist layer vertical positions. A propagation of error analysis created by the partial derivatives of a function can reveal the impacts of variable errors on the function (Ku 1966). The inflow moisture error at 850 hPa (mixing ratio bias of $\sim+7.2\times10^{-4}\,\mathrm{kg\,kg^{-1}}$) combined with error in 850-hPa temperature leads to an 850-hPa equivalent potential temperature (θ_e) bias of $\sim+2$ K, where ~1.9 K of the bias is due to moisture error alone. The model has more latent heating due to this error, which increases updraft speeds.
5) Inflow meridional wind MB below 700 hPa is near $-3\,\mathrm{m\,s^{-1}}$, indicating that inflow wind speeds are underestimated in the ensemble analyses. A propagation of error calculation (Ku 1966) for surface–500-hPa vertical wind shear given an inflow meridional surface wind bias of $\sim-4.8\,\mathrm{m\,s^{-1}}$ reveals that this error only contributes to $-0.16\,\mathrm{m\,s^{-1}}$ of the inflow shear bias. Thus, the majority of wind shear error likely originates from midlevel (500 hPa) wind error. This notion deserves further study.
6) Within the upper troposphere between 300 and 150 hPa, both horizontal wind components have large RMSDs. Upper-level wind MB are present in all near-storm environment regions, but are more pronounced within anvil regions, including within the environments downstream of convection. These results suggest the model struggles to accurately depict convective alterations of the upper levels where winds have a northwesterly directional bias and speeds are underpredicted.
7) Inflow wind shear errors are largest given the larger errors of low-level horizontal winds, particularly the v-wind component.

Although analysis errors are large in some regions surrounding the observed areas of deep convection, the analyses created by radar and conventional data assimilation depict convective near-storm environments that agree reasonably well with the upsonde observations and suggest that model analyses are a trustworthy source for insight into how deep convection alters the nearby environment. Convective-scale model analyses are therefore a suitable tool to assess the mesoscale feedbacks due to convective storms, which could affect further convection evolution. However, even more extensive near-storm observations are required to truly evaluate the impact of convection on its surrounding environment, particularly within inflow and outflow regions. Other simulations with varying microphysics schemes would evaluate cold pool strength and depth sensitivity.

Acknowledgments. The authors are very grateful for assistance with NEWS-e configuration from Dusty Wheatley, Kent Knopfmeier, Thomas Jones, and Gerry Creager of the CIMMS/NSSL Warn-on-Forecast group. Many thanks to Stacey Hitchcock for sharing upsonde processing scripts. Fruitful discussions were had with Ryan Sobash, Glen Romine, and Morris Weisman of NCAR. Two anonymous reviewers greatly enhanced the presentation of these results. Mike Coniglio and

Jack Kain of NSSL also reviewed and improved this manuscript. This study was supported by NSF Grant AGS-1230114. Last, the authors would like to acknowledge high-performance computing support from Yellowstone (ark:/85065/d7wd3xhc) provided by NCAR's Computational and Information Systems Laboratory, sponsored by the National Science Foundation. Preprocessing for this study was performed at the OU Supercomputing Center for Education and Research (OSCER) at the University of Oklahoma (OU). The third author is supported by Grants AGS-1359703 and AGS-1046081.

REFERENCES

Aksoy, A., D. Dowell, and C. Snyder, 2009: A multicase comparative assessment of the ensemble Kalman filter for assimilation of radar observations. Part I: Storm-scale analyses. *Mon. Wea. Rev.*, **137**, 1805–1824, doi:10.1175/2008MWR2691.1.

——, ——, and ——, 2010: A multicase comparative assessment of the ensemble Kalman filter for assimilation of radar observations. Part II: Short-range ensemble forecasts. *Mon. Wea. Rev.*, **138**, 1273–1292, doi:10.1175/2009MWR3086.1.

Anabor, V., D. J. Stensrud, and O. L. L. de Moraes, 2009: Simulation of a serial upstream-propagating mesoscale convective system event over southeastern South America. *Mon. Wea. Rev.*, **137**, 2144–2163, doi:10.1175/2008MWR2617.1.

Anderson, J. L., 2001: An ensemble adjustment filter for data assimilation. *Mon. Wea. Rev.*, **129**, 2884–2903, doi:10.1175/1520-0493(2001)129<2884:AEAKFF>2.0.CO;2.

——, 2007: An adaptive covariance inflation error correction algorithm for ensemble filters. *Tellus*, **59A**, 210–224, doi:10.1111/j.1600-0870.2006.00216.x.

——, T. Hoar, K. Raeder, H. Liu, N. Collins, R. Torn, and A. Avellano, 2009: The Data Assimilation Research Testbed: A community facility. *Bull. Amer. Meteor. Soc.*, **90**, 1283–1296, doi:10.1175/2009BAMS2618.1.

Bluestein, H. B., J. C. Snyder, and J. B. Houser, 2015: A multiscale overview of the El Reno, Oklahoma, tornadic supercell of 31 May 2013. *Wea. Forecasting*, **30**, 525–552, doi:10.1175/WAF-D-14-00152.1.

Brooks, H. E., C. A. Doswell III, and J. Cooper, 1994: On the environments of tornadic and nontornadic mesocyclones. *Wea. Forecasting*, **9**, 606–618, doi:10.1175/1520-0434(1994)009<0606:OTEOTA>2.0.CO;2.

Cintineo, R. M., and D. J. Stensrud, 2013: On the predictability of supercell thunderstorm evolution. *J. Atmos. Sci.*, **70**, 1993–2011, doi:10.1175/JAS-D-12-0166.1.

Clark, A. J., W. A. Gallus Jr., M. Xue, and F. Kong, 2010a: Growth of spread in convection-allowing and convection-parameterizing ensembles. *Wea. Forecasting*, **25**, 594–612, doi:10.1175/2009WAF2222318.1.

——, ——, ——, and ——, 2010b: Convection-allowing and convection-parameterizing ensemble forecasts of a mesoscale convective vortex and associated severe weather environment. *Wea. Forecasting*, **25**, 1052–1081, doi:10.1175/2010WAF2222390.1.

Coniglio, M. C., J. Correia Jr., P. T. Marsh, and F. Kong, 2013: Verification of convection-allowing WRF Model forecasts of the planetary boundary layer using sounding observations. *Wea. Forecasting*, **28**, 842–862, doi:10.1175/WAF-D-12-00103.1.

Cressman, G. P., 1959: An operational objective analysis system. *Mon. Wea. Rev.*, **87**, 367–374, doi:10.1175/1520-0493(1959)087<0367:AOOAS>2.0.CO;2.

Dowell, D. C., and L. J. Wicker, 2009: Additive noise for storm-scale ensemble forecasting and data assimilation. *J. Atmos. Oceanic Technol.*, **26**, 911–927, doi:10.1175/2008JTECHA1156.1.

——, F. Zhang, L. J. Wicker, C. Snyder, and N. A. Crook, 2004: Wind and temperature retrievals in the 17 May 1981 Arcadia, Oklahoma, supercell: Ensemble Kalman filter experiments. *Mon. Wea. Rev.*, **132**, 1982–2005, doi:10.1175/1520-0493(2004)132<1982:WATRIT>2.0.CO;2.

Engerer, N. A., D. J. Stensrud, and M. C. Coniglio, 2008: Surface characteristics of observed cold pools. *Mon. Wea. Rev.*, **136**, 4839–4849, doi:10.1175/2008MWR2528.1.

Fritsch, J. M., and R. A. Maddox, 1981a: Convectively driven mesoscale pressure systems aloft. Part I: Observations. *J. Appl. Meteor.*, **20**, 9–19, doi:10.1175/1520-0450(1981)020<0009:CDMWSA>2.0.CO;2.

——, and ——, 1981b: Convective driven mesoscale weather systems aloft. Part II: Numerical simulations. *J. Appl. Meteor.*, **20**, 20–26, doi:10.1175/1520-0450(1981)020<0020:CDMWSA>2.0.CO;2.

Gaspari, G., and S. E. Cohn, 1999: Construction of correlation functions in two and three dimensions. *Quart. J. Roy. Meteor. Soc.*, **125**, 723–757, doi:10.1002/qj.49712555417.

Hitchcock, S. M., M. C. Coniglio, and K. H. Knopfmeier, 2016: Impact of MPEX upsonde observations on ensemble analyses and forecasts of the 31 May 2013 convective event over Oklahoma. *Mon. Wea. Rev.*, **144**, 2889–2913, doi:10.1175/MWR-D-15-0344.1.

Hong, S.-Y., S. Y. Noh, and J. Dudhia, 2006: A new vertical diffusion package with an explicit treatment of entrainment processes. *Mon. Wea. Rev.*, **134**, 2318–2341, doi:10.1175/MWR3199.1.

Johnson, A., X. Wang, J. R. Carley, L. J. Wicker, and C. Karstens, 2015: A comparison of multiscale GSI-based EnKF and 3DVar data assimilation using radar and conventional observations for midlatitude convective-scale precipitation forecasts. *Mon. Wea. Rev.*, **143**, 3087–3108, doi:10.1175/MWR-D-14-00345.1.

Jones, T. A., K. Knopfmeier, D. Wheatley, G. Creager, P. Minnis, and R. Palikondo, 2016: Storm-scale data assimilation and ensemble forecasting with the NSSL experimental Warn-on-Forecast system. Part II: Combined radar and satellite data experiments. *Wea. Forecasting*, **31**, 297–327, doi:10.1175/WAF-D-15-0107.1.

Kain, J. S., S. J. Weiss, J. J. Levit, M. E. Baldwin, and D. R. Bright, 2006: Examination of convective allowing configurations of the WRF model for the prediction of severe convective weather: The SPC/NSSL spring program 2004. *Wea. Forecasting*, **21**, 167–181, doi:10.1175/WAF906.1.

——, and Coauthors, 2008: Some practical considerations regarding horizontal resolution in the first generation of operational convection-allowing NWP. *Wea. Forecasting*, **23**, 931–952, doi:10.1175/WAF2007106.1.

Keyser, D. A., and D. R. Johnson, 1984: Effects of diabatic heating on the ageostrophic circulation of an upper tropospheric jet streak. *Mon. Wea. Rev.*, **112**, 1709–1724, doi:10.1175/1520-0493(1984)112<1709:EODHOT>2.0.CO;2.

Ku, H. H., 1966: Notes on the use of propagation of error formulas. *J. Res. Natl. Bur. Stand.*, **70C**, 263–273.

Leary, C. A., 1979: Behavior of the wind field in the vicinity of a cloud cluster in the intertropical convergence zone. *J. Atmos. Sci.*, **36**, 631–639, doi:10.1175/1520-0469(1979)036<0631:BOTWFI>2.0.CO;2.

Maddox, R. A., 1980: Mesoscale convective complexes. *Bull. Amer. Meteor. Soc.*, **61**, 1374–1387, doi:10.1175/1520-0477(1980)061<1374:MCC>2.0.CO;2.

Majcen, M., P. Markowski, Y. Richardson, D. Dowell, and J. Wurman, 2008: Multipass objective analyses of Doppler radar data. *J. Atmos. Oceanic Technol.*, **25**, 1845–1858, doi:10.1175/2008JTECHA1089.1.

Metz, N. D., and L. F. Bosart, 2010: Derecho and MCS development, evolution, and multiscale interactions during 3–5July 2003. *Mon. Wea. Rev.*, **138**, 3048–3070, doi:10.1175/2010MWR3218.1.

Ninomiya, K., 1971a: Dynamical analysis of outflow from tornado-producing thunderstorms as revealed by ATS III pictures. *J. Appl. Meteor.*, **10**, 275–294, doi:10.1175/1520-0450(1971)010<0275:DAOOFT>2.0.CO;2.

——, 1971b: Mesoscale modification of synoptic situations from thunderstorm development as revealed by ATS III and aerological data. *J. Appl. Meteor.*, **10**, 1103–1121, doi:10.1175/1520-0450(1971)010<1103:MMOSSF>2.0.CO;2.

Parker, M. D., 2014: Composite VORTEX2 supercell environments from near-storm soundings. *Mon. Wea. Rev.*, **142**, 508–529, doi:10.1175/MWR-D-13-00167.1.

Perkey, D. J., and R. A. Maddox, 1985: A numerical investigation of a mesoscale convective system. *Mon. Wea. Rev.*, **113**, 553–566, doi:10.1175/1520-0493(1985)113<0553:ANIOAM>2.0.CO;2.

Rotunno, R., J. B. Klemp, and M. L. Weisman, 1988: A theory for strong, long-lived squall lines. *J. Atmos. Sci.*, **45**, 463–485, doi:10.1175/1520-0469(1988)045<0463:ATFSLL>2.0.CO;2.

Sapucci, L. F., L. A. T. Machado, R. B. Silveira, G. Fisch, and J. F. G. Monico, 2005: Analysis of relative humidity sensors at the WMO radiosonde intercomparison experiment in Brazil. *J. Atmos. Oceanic Technol.*, **22**, 664–678, doi:10.1175/JTECH1754.1.

Skamarock, W. C., and Coauthors, 2008: A description of the Advanced Research WRF version 3. NCAR Tech. Note NCAR/TN-475+STR, 113 pp., doi:10.5065/D68S4MVH.

Smull, B. F., and J. A. Augustine, 1993: Multiscale analysis of a mature mesoscale convective complex. *Mon. Wea. Rev.*, **121**, 103–132, doi:10.1175/1520-0493(1993)121<0103:MAOAMM>2.0.CO;2.

Snyder, C., and F. Zhang, 2003: Assimilation of simulated Doppler radar observations with an ensemble Kalman filter. *Mon. Wea. Rev.*, **131**, 1663–1677, doi:10.1175//2555.1.

Sobash, R. A., and D. J. Stensrud, 2015: Assimilating surface mesonet observations with the EnKF to improve ensemble forecasts of convection initiation on 29 May 2012. *Mon. Wea. Rev.*, **143**, 3700–3725, doi:10.1175/MWR-D-14-00126.1.

——, and L. J. Wicker, 2015: On the impact of additive noise in storm-scale EnKF experiments. *Mon. Wea. Rev.*, **143**, 3067–3086, doi:10.1175/MWR-D-14-00323.1.

Stensrud, D. J., 1996: Effects of a persistent, midlatitude mesoscale region of convection on the large-scale environment during the warm season. *J. Atmos. Sci.*, **53**, 3503–3527, doi:10.1175/1520-0469(1996)053<3503:EOPMMR>2.0.CO;2.

——, and J. L. Anderson, 2001: Is midlatitude convection an active or a passive player in producing global circulation patterns. *J. Climate*, **14**, 2222–2237, doi:10.1175/1520-0442(2001)014<2222:IMCAAO>2.0.CO;2.

——, and Coauthors, 2009: Convective-scale Warn-on-Forecast system: A vision for 2020. *Bull. Amer. Meteor. Soc.*, **90**, 1487–1499, doi:10.1175/2009BAMS2795.1.

——, and Coauthors, 2013: Progress and challenges with Warn-on-Forecast. *Atmos. Res.*, **123**, 2–16, doi:10.1016/j.atmosres.2012.04.004.

Thompson, G., P. R. Field, R. M. Rasmussen, and W. R. Hall, 2008: Explicit forecasts of winter precipitation using an improved bulk microphysics scheme. Part II: Implementation of a new snow parameterization. *Mon. Wea. Rev.*, **136**, 5095–5115, doi:10.1175/2008MWR2387.1.

Tong, M., and M. Xue, 2005: Ensemble Kalman filter assimilation of Doppler radar data with a compressible nonhydrostatic model: OSS experiments. *Mon. Wea. Rev.*, **133**, 1789–1807, doi:10.1175/MWR2898.1.

Trapp, R. J., D. J. Stensrud, M. C. Coniglio, R. S. Schumacher, M. E. Baldwin, S. Waugh, and D. T. Conlee, 2016: Mobile radiosonde deployments during the Mesoscale Predictability Experiment (MPEX): Rapid and adaptive sampling of upscale convective feedbacks. *Bull. Amer. Meteor. Soc.*, **97**, 329–336, doi:10.1175/BAMS-D-14-00258.1.

Trier, S. B., and R. D. Sharman, 2009: Convection-permitting simulations of the environment supporting widespread turbulence within the upper-level outflow of a mesoscale convective system. *Mon. Wea. Rev.*, **137**, 1972–1990, doi:10.1175/2008MWR2770.1.

Weisman, M. L., and R. Rotunno, 2004: "A theory for strong, long-lived squall lines" revisited. *J. Atmos. Sci.*, **61**, 361–382, doi:10.1175/1520-0469(2004)061<0361:ATFSLS>2.0.CO;2.

——, and Coauthors, 2015: The Mesoscale Predictability Experiment (MPEX). *Bull. Amer. Meteor. Soc.*, **96**, 2127–2149, doi:10.1175/BAMS-D-13-00281.1.

Wheatley, D. M., D. J. Stensrud, D. C. Dowell, and N. Yussouf, 2012: Application of a WRF mesoscale data assimilation system to springtime severe weather events 2007–09. *Mon. Wea. Rev.*, **140**, 1539–1557, doi:10.1175/MWR-D-11-00106.1.

——, N. Yussouf, and D. J. Stensrud, 2014: Ensemble Kalman filter analyses and forecasts of a severe mesoscale convective system using different choices of microphysics schemes. *Mon. Wea. Rev.*, **142**, 3243–3263, doi:10.1175/MWR-D-13-00260.1.

——, K. H. Knopfmeier, T. A. Jones, and G. J. Creager, 2015: Storm-scale data assimilation and ensemble forecasting with the NSSL Experimental Warn-on-Forecast System. Part I: Radar data experiments. *Wea. Forecasting*, **30**, 1795–1817, doi:10.1175/WAF-D-15-0043.1.

Wolf, B. J., and D. R. Johnson, 1995a: The mesoscale forcing of a midlatitude upper-tropospheric jet streak by a simulated convective system. Part I: Mass circulation and ageostrophic processes. *Mon. Wea. Rev.*, **123**, 1059–1087, doi:10.1175/1520-0493(1995)123<1059:TMFOAM>2.0.CO;2.

——, and ——, 1995b: The mesoscale forcing of a midlatitude upper-tropospheric jet streak by a simulated convective system. Part II: Kinetic energy and resolution analysis. *Mon. Wea. Rev.*, **123**, 1088–1111, doi:10.1175/1520-0493(1995)123<1088:TMFOAM>2.0.CO;2.

Yussouf, N., and D. J. Stensrud, 2010: Impact of phased-array radar observations over a short assimilation period: Observing system simulation experiments using an ensemble Kalman filter. *Mon. Wea. Rev.*, **138**, 517–538, doi:10.1175/2009MWR2925.1.

——, E. R. Mansell, L. J. Wicker, D. M. Wheatley, and D. J. Stensrud, 2013: The ensemble Kalman filter analyses and forecasts of the 8 May 2003 Oklahoma City tornadic supercell storm using single- and double-moment microphysics schemes. *Mon. Wea. Rev.*, **141**, 3388–3412, doi:10.1175/MWR-D-12-00237.1.

——, D. C. Dowell, L. J. Wicker, K. H. Knopfmeier, and D. M. Wheatley, 2015: Storm-scale data assimilation and ensemble forecasts for the 27 April 2011 severe weather outbreak in Alabama. *Mon. Wea. Rev.*, **143**, 3044–3066, doi:10.1175/MWR-D-14-00268.1.

Zhang, F., N. Bei, R. Rotunno, C. Snyder, and C. C. Epifanio, 2007: Mesoscale predictability of moist baroclinic waves: Convection-permitting experiments and multistage error growth dynamics. *J. Atmos. Sci.*, **64**, 3579–3594, doi:10.1175/JAS4028.1.